Author Contributions:

Conceptualization: Andréa C. G. Hughes, Michael Chaffin, Edwin Mierkiewicz, Justin Deighan, Jasper Halekas, Cyril Simon Wedlund, Nicholas Schneider, Birgit Ritter, Zachary Girazian, Sonal Jain
Formal analysis: Andréa C. G. Hughes
Investigation: Andréa C. G. Hughes

Advancing Our Understanding of Martian Proton Aurora Through a Coordinated Multi-Model Comparison Campaign

Andréa C. G. Hughes[1,2,3] , **Michael Chaffin**[4] , **Edwin Mierkiewicz**[3] , **Justin Deighan**[4] , **Rebecca D. Jolitz**[4], **Esa Kallio**[5] , **Guillaume Gronoff**[6,7] , **Valery Shematovich**[8], **Dmitry Bisikalo**[8,9], **Jasper Halekas**[10] , **Cyril Simon Wedlund**[11] , **Nicholas Schneider**[4] , **Birgit Ritter**[12,13] , **Zachary Girazian**[10] , **Sonal Jain**[4] , **Jean-Claude Gérard**[12], and **Bradley Hegyi**[6,7]

[1]NASA Goddard Space Flight Center, Greenbelt, MD, USA, [2]Department of Physics & Astronomy, Howard University, Washington, DC, USA, [3]Center for Space and Atmospheric Research (CSAR) and the Department of Physical Sciences, Embry-Riddle Aeronautical University, Daytona Beach, FL, USA, [4]Laboratory for Atmospheric and Space Physics, University of Colorado, Boulder, CO, USA, [5]Department of Electronics and Nanoengineering, School of Electrical Engineering, Aalto University, Espoo, Finland, [6]NASA Langley Research Center, Hampton, VA, USA, [7]Science Systems and Application Inc., Hampton, VA, USA, [8]Institute of Astronomy of the Russian Academy of Sciences, Moscow, Russia, [9]National Center for Physics and Mathematics, Moscow, Russia, [10]Department of Physics and Astronomy, University of Iowa, Iowa City, IA, USA, [11]Space Research Institute, Austrian Academy of Sciences, Graz, Austria, [12]Royal Observatory of Belgium, Brussels, Belgium, [13]Université de Liège, LPAP – STAR Institute, Liege, Belgium

Abstract Proton aurora are the most commonly observed yet least studied type of aurora at Mars. In order to better understand the physics and driving processes of Martian proton aurora, we undertake a multi-model comparison campaign. We compare results from four different proton/hydrogen precipitation models with unique abilities to represent Martian proton aurora: Jolitz model (3-D Monte Carlo), Kallio model (3-D Monte Carlo), Bisikalo/Shematovich et al. model (1-D kinetic Monte Carlo), and Gronoff et al. model (1-D kinetic). This campaign is divided into two steps: an inter-model comparison and a data-model comparison. The inter-model comparison entails modeling five different representative cases using similar constraints in order to better understand the capabilities and limitations of each of the models. Through this step we find that the two primary variables affecting proton aurora are the incident solar wind particle flux and velocity. In the data-model comparison, we assess the robustness of each model based on its ability to reproduce a proton aurora observation. All models are able to effectively simulate the general shape of the data. Variations in modeled intensity and peak altitude can be attributed to differences in model capabilities/solving techniques and input assumptions (e.g., cross sections, 3-D vs. 1-D solvers, and implementation of the relevant physics and processes). The good match between the observations and multiple models gives a measure of confidence that the appropriate physical processes and their associated parameters have been correctly identified and provides insight into the key physics that should be incorporated in future models.

Plain Language Summary The purpose of the present study is to gain a deeper understanding of the physics and driving processes of Martian proton aurora through a comparative modeling campaign. The models involved in this study have important similarities and differences, such as the dimensionality (e.g., 3-D vs. 1-D), inputs, and relevant physics included. We separate the modeling campaign into two steps: a first step comparing the models with each other (i.e., model-model comparison), and a second step comparing the simulated model results with data from a proton aurora observation (i.e., data-model comparison) taken by the Imaging UltraViolet Spectrograph onboard the Mars Atmosphere and Volatile EvolutioN (MAVEN) spacecraft. We find that all of the models are able to effectively simulate the data in terms of shape and brightness range of the proton aurora observation. The results of this study inform our understanding of the primary influencing factors that cause variability in the Martian proton aurora profile, the effects of dynamically changing solar wind parameters on the coupled Mars-Sun auroral system, and the physical processes/constraints that should be considered in future modeling attempts of this unique phenomenon.

1. Introduction and Background

Proton aurora have been recently determined to be the most commonly observed type of aurora at Mars (Hughes et al., 2019). This form of aurora is one of three primary types of Martian aurora, in addition to discrete (Bertaux et al., 2005) and diffuse aurora (Schneider et al., 2015). Further, even though this phenomenon was theoretically

Methodology: Andréa C. G. Hughes, Michael Chaffin, Edwin Mierkiewicz, Justin Deighan, Jasper Halekas, Cyril Simon Wedlund, Nicholas Schneider, Birgit Ritter, Zachary Girazian, Sonal Jain
Project Administration: Andréa C. G. Hughes
Resources: Andréa C. G. Hughes
Supervision: Andréa C. G. Hughes, Michael Chaffin, Edwin Mierkiewicz, Justin Deighan, Jasper Halekas, Cyril Simon Wedlund, Nicholas Schneider, Birgit Ritter
Validation: Andréa C. G. Hughes, Michael Chaffin, Edwin Mierkiewicz, Justin Deighan, Jasper Halekas, Cyril Simon Wedlund, Nicholas Schneider, Birgit Ritter, Zachary Girazian, Sonal Jain
Visualization: Andréa C. G. Hughes
Writing – original draft: Andréa C. G. Hughes
Writing – review & editing: Andréa C. G. Hughes, Michael Chaffin, Edwin Mierkiewicz, Justin Deighan, Jasper Halekas, Cyril Simon Wedlund, Nicholas Schneider, Birgit Ritter

predicted by Kallio and Barabash (2001), proton aurora is the most recently discovered type of Martian aurora (Deighan et al., 2018; Ritter et al., 2018), and is thereby arguably one of the least studied and understood types of Martian aurora. Past efforts to model these phenomena have been unable to fully reproduce the observations (e.g., Deighan et al., 2018, in which the shape of the modeled profile resembled the data, but the modeled peak altitudes were consistently below the data and modeled intensities required adjustment via a scaling factor to match the data), suggesting a gap in our understanding and a need for further exploration of the underlying physics of these events through modeling.

Proton aurora can be identified in ultraviolet data as an enhancement in the hydrogen (H) Lyman-alpha (Ly-α) emission (121.6 nm) above the background coronal H brightness between an altitude of ∼110–150 km; this enhancement is due to the contribution from the proton aurora-inducing H energetic neutral atoms (ENAs) as they collide with the atmosphere and emit photons (see Figure 1 from Hughes et al., 2019 for more detail and explanation of formation processes). In a previous statistical study, Hughes et al. (2019) used multiple Mars years of data from the Imaging UltraViolet Spectrograph (IUVS) (McClintock et al., 2015) onboard the Mars Atmosphere and Volatile EvolutioN (MAVEN) spacecraft (Jakosky et al., 2015) to assess the phenomenology of Martian proton aurora. Based on this study, they found that most Martian proton aurora events occur on the dayside of the planet (i.e., at low solar zenith angles, SZAs) around the southern summer solstice (i.e., solar longitude, L_s, ∼270°). This seasonal increase in proton aurora activity was found to be correlated with the inflated Martian H corona around southern summer solstice, which corresponds with higher H column densities and H escape rates, caused by upper atmospheric temperatures and dust activity reaching an annual maximum during this time (e.g., Chaffin et al., 2014, 2021; Clarke et al., 2014; Halekas, 2017; Hughes et al., 2019). This annual variability is also coupled with slightly higher solar wind proton fluxes as Mars is near perihelion ($L_s = 251°$). The seasonally increased abundance of H beyond the planet's bow shock during this season allows a larger fraction of solar wind protons to be converted into hydrogen ENAs (H-ENAs) through charge exchange, which can then bypass the bow shock and magnetic pileup boundary to create more frequent proton aurora events with very large Ly-α emission enhancements during this time of year.

The purpose of the present study is to gain a deeper understanding of the physics and driving processes of Martian proton aurora through a comparative modeling campaign. While previous data-driven statistical studies of these aurora provided an understanding of their phenomenology, frequency, and likely driving processes, much is still lacking in our knowledge. This includes, for example, the specific effects of variability in different input parameters on the shape, brightness, and peak altitude of the proton aurora profile, as well as the influence of model capabilities, solving techniques, and input assumptions on effectively simulating proton aurora observations. Modeling proton aurora activity provides an opportunity to understand these events, as it allows us to constrain different input parameters and predict variations in the results. Moreover, by undertaking a comparative modeling campaign in which the results of multiple models are evaluated (with each model emphasizing specific physical processes and utilizing different numerical solving techniques), we are able to simultaneously explore the range of possible outcomes for individual auroral events. We note that the statistical study by Hughes et al. (2019) incorporated data from only the first ∼two Mars years of MAVEN orbits, taken during the declining and minimum portion of the solar cycle. While the Hughes et al. (2019) study encompassed many proton aurora events, in this study we focus our efforts on modeling one specific event from the IUVS dataset that exhibited particularly interesting proton aurora activity.

Being able to effectively model Martian proton aurora is necessary for developing our understanding of observations of auroral events in the IUVS dataset, as well as the ability to predict and understand future observations. The purpose of this modeling campaign is not to determine which model is the "best" proton/hydrogen precipitation model in our study, but rather to identify the distinct capabilities each model provides in simulating proton/hydrogen precipitation at Mars. Through undertaking a rigorous assessment of Martian proton aurora using the results of multiple different simulations, we are able to develop an understanding of the gaps in our knowledge and improve our abilities to more effectively model future proton aurora observations.

2. Modeling Campaign Description

2.1. Campaign Outline/Steps

In order to accomplish the goals of this study, this campaign is divided into two primary steps: an inter-model comparison step (Step 1) and a data-model comparison step (Step 2). Each step is subdivided to reflect the "native

format" (i.e., original model outputs) and "forward-modeled" results (i.e., the results of running the modeled outputs through a radiative transfer model, described in more detail below); these sub-steps are referred to as Steps 1-A and 1-B, as well as Steps 2-A and 2-B. In the following sections we describe the models and discuss the results of each of these steps. We also consider the assumptions of each model and compare differences in the model capabilities that may impact the results.

2.2. Models and Modeling Teams Involved in Campaign

In this study, we utilize four different proton/hydrogen precipitation models and one radiative transfer model. In the following sections, we briefly discuss the different models and teams involved. Detailed descriptions of each of the four proton/hydrogen precipitation models used in the study and an overview table comparing their cross-section assumptions are provided in supplementary material (Text S1–S4 and Table S1 in Supporting Information S1). A radiative transfer (RT) model is then used to "forward-model" the results of each step into observation space (i.e., Steps 1-B and 2-B, respectively); this model is also briefly described below.

2.2.1. Proton/Hydrogen Precipitation Models

We include four unique proton/hydrogen precipitation models in this study: the Jolitz model (i.e., "ASPEN"), the Kallio model, the Bisikalo/Shematovich et al. model, and the Gronoff et al. model (i.e., "Aeroplanets"). The former three are Monte Carlo models (with the Jolitz and Kallio models being 3-dimensional (3-D) and the Bisikalo/Shematovich et al. model being 1-D). A Monte Carlo simulation is a numerical technique that generates a range of possible outcomes and probabilities of occurrence for specific representative inputs. In such a simulation, a mathematical model is first constructed and then iteratively run using different random input variables; the results can be considered in the context of a probability distribution curve and are averaged together to estimate the most likely outcome. In contrast, the Gronoff et al. model uses a 1-D Kinetic scheme, based on a semi-analytical treatment of the coupled H^+/H Boltzmann kinetic transport equation.

2.2.1.1. Jolitz 3-D Monte Carlo Model ("ASPEN")

The Jolitz model, ASPEN (Atmospheric Scattering of Protons, Electrons, and Neutrals), is a 3-D Monte Carlo test particle simulation. This model was initially developed to predict atmospheric ionization rates at Mars by solar energetic particles, which have higher energies than the ENAs studied in this paper (Jolitz et al., 2017), and has since been used to predict precipitating SEP electron fluxes at Mars (Jolitz et al., 2021). The model solves the Lorentz force equations for energetic particle motion and uses a Monte Carlo approach to predict collisions and resulting energy loss in the atmosphere.

Using ASPEN, stochastic collisions are modeled by inverting the relation between intensity, density, and absorption cross section for a particle beam incident on a medium of scatterers (colloquially known as Beer's law) to dynamically calculate a probability distribution function that is combined with a random number to predict variable distances between collisions. This probability distribution function is calculated for each individual particle and depends on the position, path, and energy through the planetary atmosphere. Similarly, whenever a collision occurs, the type of collision is predicted probabilistically using the relative cross section of each possible collisional process, and the particle energy is decremented by the corresponding energy loss. As a particle loses energy, the relative cross sections of each process change.

This model (as well as all models in this study) is highly dependent on the choice of cross sections. For the application in this study, the selected cross sections for hydrogen and proton impact on carbon dioxide are described in Jolitz et al. (2017), with one exception: the cross sections for proton- and hydrogen-impact excitation was replaced with Ly-α emission cross sections. ASPEN uses a cross section calculated by scaling the corresponding emission cross sections from impact on molecular oxygen.

Since ASPEN is a 3-D Monte Carlo simulation, predicting an accurate emission rate requires appropriate choice of initial conditions and a large volume of simulated particles. For Step 1, we simulate 10,000 particles incident on the subsolar point from an altitude of 600 km and calculate the emission rate by binning all Ly-α emitting collisions as a function of altitude and multiplying by the incident flux. For Step 2, we simulate 10,000 particles uniformly distributed in space on a plane perpendicular to the direction of solar wind flow. Each particle represents a fraction of the assumed incident flux. The emission rate was then calculated by weighing the total number of emissions binned by altitude, solar zenith angle, and the fraction of flux associated with each simulated particle.

2.2.1.2. Kallio 3-D Monte Carlo Model

The Kallio model is a 3-D Monte Carlo model where the incident particle, either H^+ or H, collides with neutral particles, after which the velocity of the particle is changed. The model includes 6 elastic and 24 inelastic processes; however, in this study, only the processes mentioned in the main text of this paper were used.

The model inputs are neutral atom densities, energy dependent total cross sections, the differential scattering cross sections (DSCS), the number of precipitating particles (5,000 particles in the Step 1 runs and 100,000 particles in Step 2 runs), and the initial positions and velocities of the precipitating particles (in the present case, hydrogen atoms). The total cross sections are given in Kallio and Barabash (2001, Table 1 and Figure 3), and the DSCS scattering angle distribution in Kallio and Barabash (2000, Figure 1, "nominal") and Kallio and Barabash (2001, Figure 2). Total cross sections give the probability that a collision occurs. Random numbers are used to model if a collision occurs, and which collision process occurs. If a collision happens, then the DSCS determines the new velocity of the incident particle after collision. The value of the scattering angle is obtained by using a new random variable.

The largest uncertainty for the obtained Ly-α volume emission rate (VER) is related to the uncertainty of the total cross sections used and the DSCS between H and H^+ particles and CO_2 molecules. In the simulation, many of these H/H^+ collisions with CO_2 are modeled with H/H^+ collisions with O_2 and N_2, which was published in the literature (see Kallio & Barabash, 2001, Table 1, for details).

In the simulation, particles are injected into the upper atmosphere at the point $[x, y, z] = [260 \text{ km} + R_{Mars}, 0, 0]$, where the radius of Mars, R_{Mars}, is 3,393 km. Following the methodology of Kallio and Barabash (2000, 2001), the model saves the position and the velocity of the particle if it has a Ly-α collision process. The Ly-α volume production rate is derived from the saved positions of Ly-α processes by collecting the number of the Ly-α collision processes at a given altitude range. Then the Ly-α volume emission is derived by using a 1-D approximation, which assumes that the area of the emission perpendicular to the x-axis is equal to the initial area in the solar wind through which the precipitating particles initially came. In the plots presented in this paper, the Ly-α emission altitude profiles are derived in 1 km altitude bins.

2.2.1.3. Bisikalo/Shematovich et al. 1-D Monte Carlo Model

The Bisikalo/Shematovich et al. model is a 1-D Monte Carlo model. The model considers three primary processes: (a) precipitation of high-energy hydrogen atoms and protons that lose their kinetic energy in the elastic and inelastic collisions, (b) ionization of target atmospheric molecules/atoms, and (c) charge transfer and electron capture collisions with the major atmospheric constituents (i.e., CO_2, N_2, and O). Secondary fast hydrogen atoms and protons carry enough kinetic energy to cycle through the collisional channels mentioned above and result in a growing set of translationally and internally excited atmospheric atoms and/or molecules.

To study the precipitation of high-energy H/H^+ flux into the planetary atmosphere, we use the kinetic Monte Carlo model to solve the kinetic Boltzmann equations (Gérard et al., 2000; Shematovich et al., 2011) for H^+ and H. The model is 1-D in geometric space and 3-D in velocity space. Nevertheless, the 3-D trajectories of H/H^+ are calculated in the code with final projection onto the radial direction. The current version of the Monte Carlo model (Shematovich et al., 2019) incorporates the full structure of the induced magnetic field of Mars; that is, all three components of the magnetic field $\mathbf{B} = \{Bx, By, Bz\}$ are taken into account. The details of the model implementation and statistics control with the variance below 10% can be found in Shematovich et al. (2019).

The essence of the kinetic Monte Carlo model is accounting for all possible collisions in the atmospheric region studied. Therefore, statistics for all collisional processes are accumulated during the numerical realization of the kinetic model of the proton aurora. It provides a good basis for the evaluation of the Ly-α source functions as keeping all excitation processes and their spatial characteristics makes it possible to determine the statistical distribution of the emitted Ly-α photons.

A key aspect of this model is the probabilistic treatment of the scattering angle distribution, which influences both the energy degradation rate and the angular redistribution of the precipitating protons and hydrogen atoms (Bisikalo et al., 2018; Shematovich et al., 2019). The model utilizes both total and differential cross sections when calculating the post-collision velocities for high-energy precipitating H/H^+ and atmospheric particles.

The region under study is limited by the lower boundary, which is placed at 80 km, where H/H^+ particles are efficiently thermalized. The upper boundary is set at 500 km, where measurements or calculations of the precipitating fluxes of protons or hydrogen atoms are used as a boundary condition. Both table and/or analytic (Maxwellian

and/or kappa-distribution) functions representing the energy spectra as well as the pitch-angle (monodirectional, isotropic, or limited by cone) distributions of precipitating particles could be used at the upper boundary.

2.2.1.4. Gronoff et al. 1-D Kinetic Model ("Aeroplanets")

The Gronoff et al. model, called Aeroplanets, utilizes a 1-D kinetic transport approach. Aeroplanets (Gronoff, Simon Wedlund, Mertens, Barthélemy, et al., 2012; Gronoff, Simon Wedlund, Mertens, & Lillis, 2012; Simon Wedlund et al., 2011) is based on an auroral particle precipitation model initially developed for the Earth and later adapted to Mars (as well as numerous other planetary bodies, e.g., Venus and Titan). This model computes the ionization and excitation of atmospheric species by photon, electron, proton, and cosmic ray impacts, including the effect of secondary particles. The proton transport module within Aeroplanets is based on the work of Galand et al. (1998, 1997), Simon (2006), and Simon et al. (2007) for Earth, who solved semi-analytically the coupled proton-hydrogen dissipative kinetic transport equation for protons and hydrogen atoms charge-changing with neutral gas. It was originally developed from the idea that dissipative forces responsible for angular redistributions due to elastic scattering can be introduced in the force term of the general dissipative Boltzmann equation (Galand et al., 1997). As such, angular redistributions due to magnetic mirroring effects and collisions are naturally included, leading to backscattering.

Inputs to the Aeroplanets model include cross sections, the vertical profile of atmospheric neutral densities (i.e., composition at different altitudes), and the precipitating fluxes of particles such as H and H^+ at the top of the atmosphere (any shape and energy distribution can be prescribed). Outputs include the vertical profile of H and H^+ differential energy fluxes, and the vertical profile of the production rate of excited and ionized species and electrons, including emissions. Simulations are performed on a grid typically spanning 90–250 km, which corresponds approximately to the exobase level.

Cross sections in Aeroplanets are taken from the latest version of the Atomic and Molecular Cross section for Ionization and Aurora Database (ATMOCIAD) (Gronoff et al., 2021) cross section and reaction rate database compiled and developed by Simon Wedlund et al. (2011) and Gronoff, Simon Wedlund, Mertens, and Lillis (2012). In ATMOCIAD, experimental and theoretical cross sections as well as their uncertainties are collected. Although ATMOCIAD is an extensive collection of cross sections, we note that there is still a rather poor characterization of cross sections at low energies (typically in the sub-keV range). Regarding differential cross sections, Aeroplanets uses phase functions that are convolved with the energy-dependent cross sections described above.

Aeroplanets is well qualified for the fast computation of the proton precipitation from a measured spectra near the planet, and for the fast computation of the total ionization and excitations rates initiated by that precipitation thanks to its coupling with a secondary electron transport model. The analytic computation approach prevents the computation within very complex magnetic topologies (which are best handled by Monte-Carlo models) but is suited for handling large sets of initial angles and energies.

2.2.2. Radiative Transfer Model

To quantitatively compare the proton aurora modeling results and the IUVS limb observations, it is necessary to perform a radiative transport calculation (done in this study using a Radiative Transfer model created by coauthor Deighan). While the Ly-α emission from thermal hydrogen is optically thick in the upper atmosphere of Mars (Anderson & Hord, 1971), the emission associated with proton aurora can be considered optically thin due to the large Doppler shifting caused by the high velocity of the ENAs (Gérard et al., 2019). This both offsets the line center and broadens the width of the spectral line shape and ensures that few of the photons produced by proton aurora interact with the ambient thermal hydrogen population for most viewing geometries. This allows a simple line-of-sight integration to be employed, though CO_2 absorption must still be taken into account (Deighan et al., 2018; Gérard et al., 2019).

The procedure used to calculate a model brightness to compare with each measurement by IUVS is as follows: First, the model atmosphere is sampled at 1 km intervals starting from the reconstructed spacecraft position and extending out 3,000 km along the line-of-sight vector. This ensures adequate sampling of the model VER, as the auroral emission typically has a scale height of the order of 10 km and a peak VER occurring 500–1,700 km away from the spacecraft for IUVS periapsis limb scans. The column of CO_2 between the spacecraft and each sample point in the model is then integrated and an absorption optical depth is obtained using an absorption cross section of 7.348×10^{-20} cm^2 (Huestis & Berkowitz, 2010). The Beer-Lambert law is then applied to find

Table 1
Representative Inputs for the Five Example Cases in the Inter-Model Comparison Step (Step 1)

	Case 1 (baseline w/H-ENAs)	Case 2 (baseline w/Protons)	Case 3 (small flux)	Case 4 (high velocity)	Case 5 (hot atmosphere)
v [km/s]	400	400	400	800	400
$F_{H\text{-}ENA}$ [cm^{-2} s^{-1}]	10^7	0	10^6	10^7	10^7
F_{proton} [cm^{-2} s^{-1}]	0	10^7	0	0	0
CO$_2$ density profile (varying temp.)	CO$_2$ profile @ $T = 190$ K	CO$_2$ profile @ $T = 190$ K	CO$_2$ profile @ $T = 190$ K	CO$_2$ profile @ $T = 190$ K	CO$_2$ profile @ $T = 240$ K

Note. These parameters were varied to assess their relative importance in each model.

the attenuation caused by CO$_2$ absorption for each sample point, and the attenuated VER is integrated to obtain a column emission rate (CER). This is readily converted into the brightness unit of Rayleighs (R) conventionally used for airglow and aurora (Hunten et al., 1956). The proton aurora VER and CO$_2$ densities are both assumed to have spherical symmetry (primarily driven by the use of 1-D profiles), and the brightness calculation itself is performed using an integration through 3-D space along each line of sight.

3. Inputs and Results for Inter-Model Comparison (Step 1)

3.1. Purpose and Description of Step 1

We begin the campaign with an inter-model comparison in Step 1 using multiple different test cases of representative inputs to represent varying proton aurora conditions. The purpose of this step is to set a baseline for inter-model comparisons and to compare the effects of varying input conditions on the results of each individual model.

We use five different representative proton aurora conditions, each with varying solar wind velocity, H-ENA and proton fluxes at the top of the atmosphere, and CO$_2$ density profiles for high and low atmospheric temperature conditions (Table 1). Using these inputs, altitude versus Ly-α VER profiles were created by each model for each representative test case. In Step 1-A, we first compare the results in each modeler's native format (e.g., VER). In Step 1-B, the results are forward-modeled into observation space using the radiative transfer model. In Section 5, we discuss possible causes for the observed inter-model discrepancies.

3.2. Assumptions/Constraints for Step 1

To accurately compare the driving physics incorporated in each of the models, we implement a number of constraints on each model in Step 1 (i.e., the inter-model comparison step). The three primary constraints are (a) assuming the incident solar wind particle beam (either purely H or purely H$^+$) is monoenergetic; (b) assuming purely 1-D anti-sunward solar wind particle movement (i.e., monodirectional) incident at the subsolar point (i.e., SZA = 0°); and (c) requiring that the same cross-section processes be included in each model (yet allowing the use of different cross-section values; see Section 5.1 and Table S1 in Supporting Information S1 for more details). We empirically justify inclusion of the first two constraints based on previous observations of penetrating protons showing a monoenergetic population (i.e., typically the same energy as the solar wind) that is incident across the entire sunward-facing side of the planet (Halekas et al., 2015). For the third constraint, we specifically consider five cross-section processes for protons and/or H interacting with CO$_2$: elastic, charge exchange/electron capture, electron stripping, ionization, and Ly-α. Although all models have the ability to incorporate additional processes (see Table S1 in Supporting Information S1), most have incorporated exclusively these five processes. We note that the Bisikalo/Shematovich et al. team also included cross-section processes for Hydrogen Balmer-alpha and -beta; however, this inclusion produces only a very minor effect on the resulting VER due to the relatively small cross sections of these processes. Each modeling team also incorporated their own DSCS values (Table S1 in Supporting Information S1). Lastly, while the Jolitz and Kallio models use similar 1 km linear altitude bins, the other two models utilize different types of altitude binning. We note however, that a comparison of the type and spatial resolution of the altitude bins used by the Gronoff et al. model found that this parameter to have a negligible effect on the simulation results.

3.3. Representative Inputs for Step 1

In undertaking the inter-model comparison, we create five representative proton aurora events to be simulated by each model (Table 1). We select baseline cases that resemble previous observations of the particle flux, velocity, and neutral CO$_2$ temperature of Martian proton aurora (e.g., Deighan et al., 2018), and incrementally change the input parameters in each case in order to quantify the effect of the parameters on the proton aurora profile. In the two baseline cases we vary the type of incident particle at the top of the model atmosphere (i.e., 100% H-ENAs or 100% protons in Case 1 and Case 2, respectively); in subsequent cases we vary the average incident particle beam flux (Case 3), the particle velocity (Case 4), and the neutral atmospheric temperature (Case 5). By changing the temperature in Case 5, we also modify the scale height, and thereby the CO$_2$ density profile. In Step 1 we do not include any representative cases that consider variability associated with magnetic fields or SZAs (i.e., the
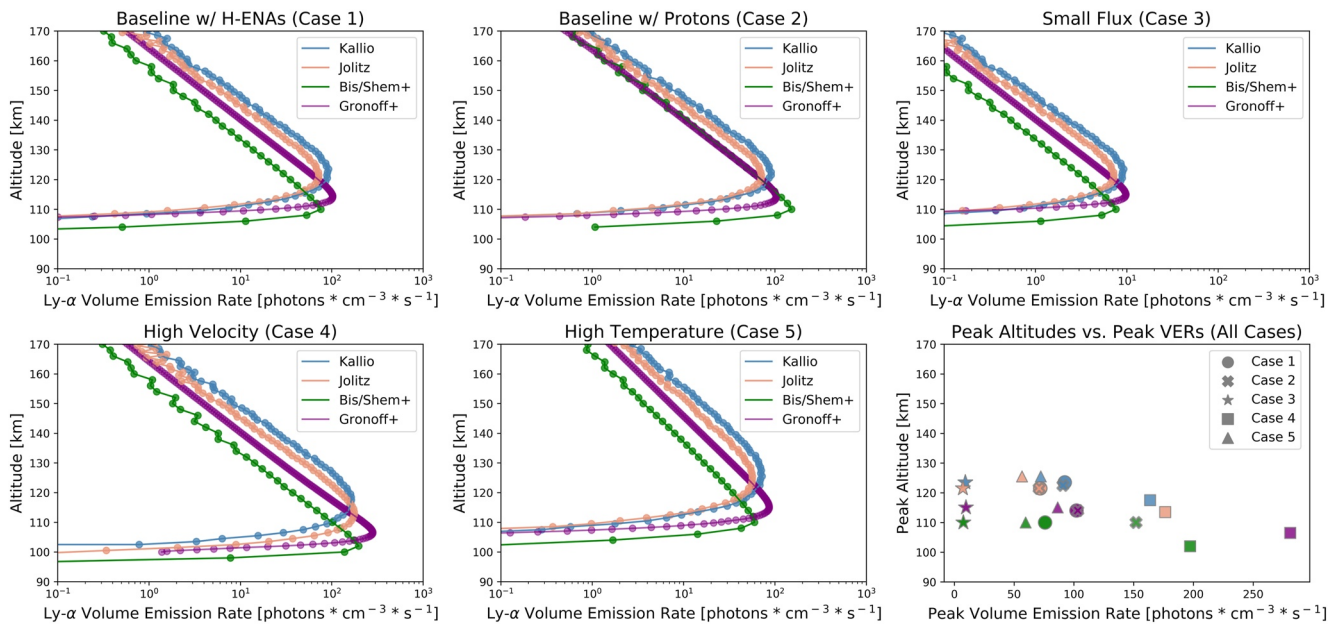
Figure 1. Simulated Lyman-α volume emission rates (VERs) of proton aurora at different altitudes from each model in this study for the five representative input cases in the inter-model comparison step of the campaign (Step 1-A). The two input parameters that have the most significant effect on the results are the incident solar wind flux and velocity. The results of this step are summarized in the bottom right plot, which presents the peak altitudes and peak VERs for each of the different cases (represented by marker style) and models (represented by color, as shown in other subplot legends). See Table 1 for the input parameters used in each of the five representative cases.

models simulate particle incidence at the subsolar point, where the Ly-α intensities are highest on the planet). While these constraints are not necessarily indicative of the actual Mars-solar wind interactions, they represent simplified scenarios that are beneficial for gauging inter-model variability. We note that in this study we are exclusively interested in modeling the proton aurora profile under different input conditions; since proton aurora are almost entirely formed due to interactions between the incident particles and the neutral CO_2 atmosphere, the model results do not directly incorporate processes occurring in the extended corona upstream of the bow shock (e.g., charge exchange between solar wind protons and the H corona; however, all but Case 2 implicitly include this process).

In order to vary the neutral atmospheric temperature parameter in the models (Case 5) we create two different CO_2 density profiles, each containing altitude-binned (1 km bin) representative CO_2 number density values for the two respective temperature ranges of 190 K (i.e., baseline temperature) and 240 K (i.e., high temperature). These different CO_2 density values were created using a standard barometric isothermal atmosphere described by the equation:

$$n(z) = n_{\mathrm{ref}} \exp\left(-\frac{(z - z_{\mathrm{ref}})}{H}\right), \tag{1}$$

where z is altitude, n_{ref} is the number density at a reference altitude, z_{ref} is the chosen reference altitude (in this case, 120 km), and H is the CO_2 scale height. Here we assume $n_{\mathrm{ref}} = 1 \times 10^{11}$ cm^{-3} at 120 km, and H is calculated for each temperature range using a value of $g = 3.46$ m/s^2 (i.e., g at the reference altitude of 120 km). The calculated scale height values for the low and high temperature cases were 10.4 and 13.1 km, respectively.

3.4. Results of Step 1-A

The results of the inter-model comparison in Figure 1 show many similarities between the different modeled proton aurora VERs, with the results of the Jolitz and Kallio models exhibiting the most similarities. Interestingly, most models predict similar trends in the relative changes observed between each of the five representative cases. There is a large range in the proton aurora peak altitudes between the models, with the Bisikalo/Shematovich et al. model consistently predicting the lowest peak altitudes and the Gronoff et al. model predicting the second
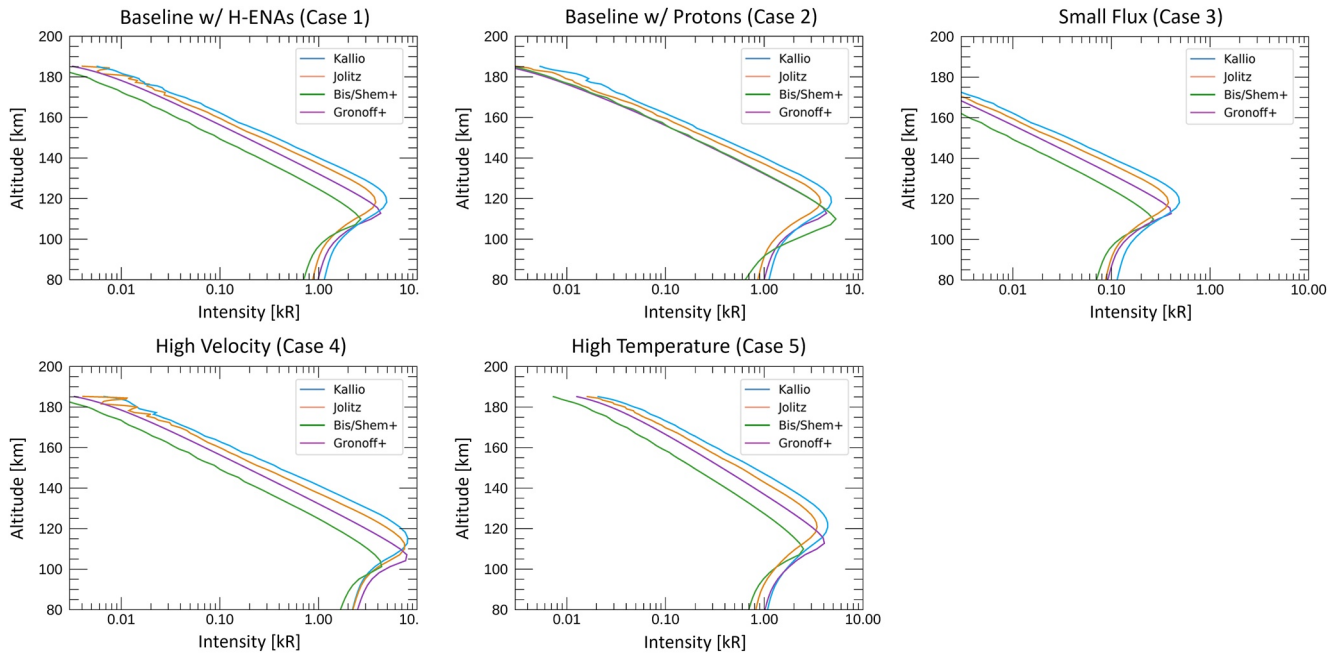
Figure 2. Simulated Ly-α intensities from the inter-model comparison after running the results of Step 1-A through the radiative transfer (RT) model (Step 1-B), which forward-models the results into observation space (e.g., performs a "line-of-sight" integration comparison). The model results more closely resemble each other after this step, but the dominant influencing factors identified in Step 1-A (Figure 1) are still present. See Table 1 for the input parameters used in each of the five representative cases.

lowest. The peak altitudes in the Jolitz and Kallio models are consistent with each other in nearly every case, with the exception of the high velocity case (Case 4), where the Jolitz model predicts a slightly lower peak altitude than the Kallio model. The Gronoff et al. model also consistently predicts the largest peak VERs in each case (with the exception of Case 2, where the Bisikalo/Shematovich et al. model predicts the largest peak VERs). Almost all of the models show no difference in the proton aurora profile (i.e., VER or altitude) based on varying the type of incident particle at the top of the atmosphere (i.e., H-ENA or proton, compare Case 1 and Case 2 profiles); the only notable exception being the Bisikalo/Shematovich et al. model, which predicts a slight increase in the VER of the proton aurora profile for protons rather than H-ENAs as the incident particle. The similarities between Cases 1 and 2 suggest that most models do not predict significant differences between a H-induced Ly-α emission and a proton-induced Ly-α emission in the proton aurora profile. The primary results of this step are summarized in the bottom right panel of Figure 1, which plots the peak altitudes versus peak VERs for each model and case.

3.5. Results of Step 1-B

In Step 1-B we forward-model the results of Step 1-A into observation space by performing a "line-of-sight" integration comparison. In this step, we produce synthetic observations that would be made by MAVEN/IUVS given the computed VERs. In so doing, the model results are converted from Ly-α VER (in units of photons/cm³ s) to Ly-α intensity (in units of kilorayleighs, kR) using the previously described radiative transfer model. Using the same radiative transfer model to forward-model each simulation's output in this step enables a more reliable cross-model comparison.

As shown in Figure 2, the results of Step 1-B further reveal similarities in the model intensities and peak altitudes for each of the five cases. We find consistently in each model that the two major variables that affect the proton aurora profile are the penetrating particle flux and the particle velocity. Decreasing the flux by an order of magnitude (Case 3) correspondingly decreases the Ly-α intensity by an order of magnitude. Similarly, doubling the particle velocity (Case 4) noticeably increases the peak intensity in each model and decreases the peak altitude by ~5–10 km. In the final representative input case of increasing the atmospheric temperature (thereby changing the neutral atmospheric scale height) (Case 5), all of the models show a slight decrease in the Ly-α peak intensity and a broadening in the profile shape at higher altitudes (i.e., the profile has a broader shape). Additionally, most
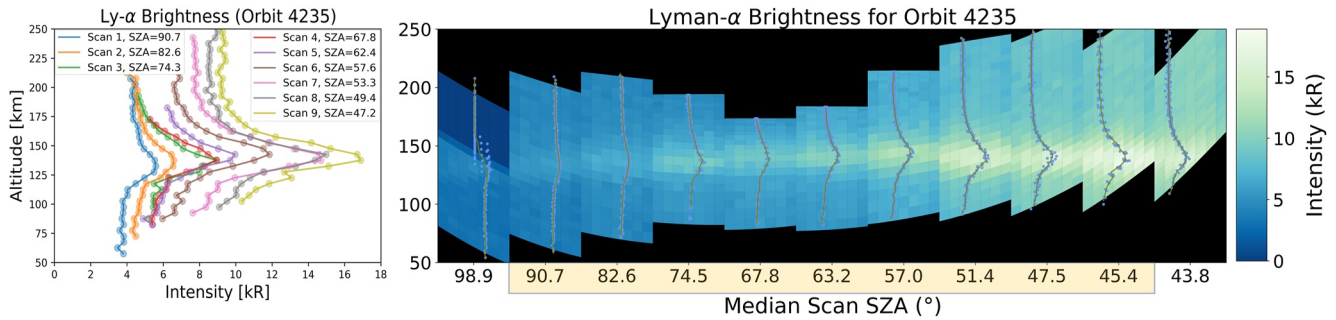
Figure 3. Imaging UltraViolet Spectrograph (IUVS) Ly-α intensity data of proton aurora observation used in the data-model portion of the campaign (Step 2). Left: IUVS Level 1C altitude-intensity profiles for limb scans used in the study (MAVEN orbit #4235); solar zenith angle (SZA) at the profile peak for each limb scan is shown in the legend. Right: Altitude-intensity profiles overlain on top of a synthetic image format of Ly-α intensities for each IUVS limb scan/mirror angle in this orbit (e.g., similar to Figure 2 from Deighan et al., 2018; see text for more details). Note that the scans are displayed as though they are contiguous but spacecraft and slit motions prevent full coverage. Only the central nine scans are used in this study (scans that are highlighted yellow at the bottom), and the SZA values shown at the bottom correspond with the median SZA for each limb scan in the orbit.

of the models show an increase in the peak altitude by ∼1–5 km in Case 5 (with the exception of the Bisikalo/Shematovich et al. model, which does not exhibit a change in the peak altitude due to the changing temperature/scale height). The differences in the profile observed in Case 5 are likely present because the VER, and therefore the unattenuated auroral brightness, scales inversely with the atmospheric scale height in order to conserve photon production in the atmosphere; this in turn causes the Ly-α brightness to appear more "spread out" across different altitudes in the proton aurora profile.

The consistency of these results between models confirms our understanding of the driving processes that have the most significant effect on the proton aurora profile. Particularly, we see in Cases 3 and 4 that the solar wind proton velocity and density (which also affect the particle energy and flux) are tremendously important in the formation of notable proton aurora events. Thus, we may extrapolate from the results that high velocity and/or density solar events, such as coronal mass ejections and corotating interaction regions, will correspondingly create significantly enhanced proton aurora events. This finding is consistent with preliminary studies of proton aurora at Mars in which the observations were found to correspond with extreme solar activity events (e.g., Ritter et al., 2018).

4. Inputs and Results for Data-Model Comparison (Step 2)

4.1. Purpose and Description of Step 2

In the second step, we assess the robustness of each of the models based on their abilities to reproduce a typical proton aurora detection from the MAVEN/IUVS dataset. In undertaking Step 2, different variables in the models were tuned to match proton aurora events in the MAVEN/IUVS dataset. The models use relevant data inputs for a specific proton aurora event to attempt to accurately reproduce the event. As in Step 1, the model results in Step 2-A are first provided in their native formats, and subsequently forward-modeled into observation space in Step 2-B using the radiative transfer model.

4.2. Description of Example Proton Aurora Event and MAVEN/IUVS Observations

For the data-model comparison stage of the campaign (Step 2), we selected an example of a proton aurora event from the MAVEN/IUVS dataset that occurred during the periapsis portion of MAVEN orbit #4235 on 3 December 2016, starting at ∼13:44 UTC. This particular proton aurora event occurred at relatively low SZAs around southern summer solstice (L_s ∼ 270°), a period of time exhibiting frequent proton aurora activity and increased dust activity associated with the concurrent Martian dust storm season. Figure 3 shows the IUVS Ly-α intensity data for this orbit. The left-hand plot of Figure 3 shows the Level 1C altitude-binned Ly-α altitude-intensity profiles for each of the limb scans used in the study. The right-hand plot of Figure 3 shows these profiles overlain on a synthetic image format of each of the IUVS limb scans from this orbit (horizontal), showing the Ly-α intensity for each of the 21 IUVS mirror integrations (vertical) and 7 spatial bins within each scan (similar to Figure 2 in Deighan et al., 2018). Note that the scans are displayed as though they are contiguous even though spacecraft and slit motions prevent full spatial

coverage. There are 11 IUVS limb scans in this orbit, but we use only the middle nine IUVS scans in this study (yellow highlighted scans in Figure 3). In evaluating the robustness of each of the models in this step of the study, the model results were compared with intensities and peak altitudes of the IUVS Ly-α profiles from these nine scans.

There are minor peak altitude variations in IUVS Ly-α observations between scans throughout this orbit. These minor altitude variations correspond to similar altitude variations in the IUVS CO_2^+ ultraviolet doublet emission ($CO_2 + B\ 2\Sigma \rightarrow X\ 2\Sigma$ around 288 nm) (not shown), suggesting the possible presence of waves and/or tides in the neutral atmosphere during this orbit (e.g., England et al., 2016; Lo et al., 2015). The likely presence of waves/tides in this orbit is strengthened by similar observations in the MAVEN/Neutral Gas and Ion Mass Spectrometer (NGIMS) inbound CO_2 altitude-density profile. We note, however, that altitude variations in the Ly-α and CO_2^+ emissions are less than 5 km, approaching the resolution limit of the observation; thus, the minor altitude variations observed in the Ly-α peak intensity or CO_2 density during this orbit should not have any significant influence on the modeled proton aurora profiles.

This particular proton aurora event exhibits an especially high orbit-mean Ly-α peak intensity and emission enhancement (11.4 and 3.93 kR, respectively) as observed by IUVS. Also notable during this orbit is a particularly high penetrating proton flux (2.73×10^6 cm^{-2} s^{-1}) observed by MAVEN's Solar Wind Ion Analyzer (SWIA) instrument (Halekas et al., 2013). SWIA observed a nominal orbit-averaged penetrating proton velocity of ~430 km/s, as well as a strong solar wind stream interaction during this orbit, resulting in an especially high penetrating proton flux. The MAVEN periapsis during this orbit was in the southern hemisphere on the dayside of the planet, with the exception of a few limb scan observations near the terminator (see Figure S1 and Figure S2 in Supporting Information S1). Because the spacecraft periapsis does not occur near any strong remanent crustal fields (Figure S1 in Supporting Information S1), we do not expect a significant influence (if any) from crustal fields during these observations. The average upstream interplanetary magnetic field (IMF) magnitude and cone angle (i.e., angle off of the Mars-Sun line) during this orbit is ~10 nT and ~45°, respectively.

4.3. Background Subtraction of Coronal H Contribution From IUVS Ly-α Brightness

The Ly-α brightness observed in the IUVS data is created by contributions from not only the nonthermal solar wind-derived H that produces proton aurora, but also from the thermalized background coronal H. Thus, by subtracting out the background coronal H from the IUVS proton aurora profiles, we are able to accurately compare the data with the model results. We perform this coronal H background subtraction by first estimating the background coronal H brightness during this time using IUVS limb scan profiles from a nearby orbit that exhibits little/less evidence of enhancement due to proton aurora activity at a similar SZA (in this case we use orbit #4229, as it exhibits the least contribution from proton aurora than any surrounding orbits). These heuristic coronal Ly-α profiles are created by fitting an arcsine function to the upper- and lower-most altitudes of the Ly-α profiles from the nearby orbit with little/less proton aurora activity. Each heuristic profile of the estimated background Ly-α brightness due to the coronal H in a given orbit is then subtracted out from each corresponding IUVS limb scan at a similar SZA from the orbit of interest containing strong evidence of proton aurora (see Figure S3 in Supporting Information S1 for Ly-α profiles before and after background subtraction and heuristic coronal background profiles used). This method is similar to the background subtraction methodology used by Deighan et al. (2018) but differs in the determination of the background coronal H profile due to the absence of nearby orbits that completely lack proton aurora, which is a consequence of the near continuous proton aurora activity during the southern summer season. The corrected intensities should then more closely reflect the H Ly-α contribution only from proton aurora. In order to determine its effectiveness, this background coronal H subtraction technique was tested on numerous other IUVS proton aurora detections and found to be a highly effective empirical method for isolating the proton aurora contribution to the IUVS Ly-α observations. However, as this methodology estimates a heuristic background coronal H by assuming minimal/no changes in the neutral atmosphere between multiple orbits, there will be inaccuracies in the corrected proton aurora profiles; we estimate these inaccuracies to be only a fraction of a kR at most.

As shown in Figure S3 in Supporting Information S1, the IUVS Ly-α intensities are reduced significantly due to this background-subtraction routine (by nearly 10 kR at low SZAs), but the shape of the profiles around the proton aurora profile peak (i.e., between ~110 and 150 km) does not change. The profile peak altitudes typically also do not change as a result of this background subtraction methodology, provided that the peak altitudes of the proton aurora orbit profiles are not significantly different from those of the background subtraction orbit profiles. However, because of a slight difference in peak altitudes between the orbit considered in this study and the orbit used for the background subtraction routine (i.e., orbit #4235 and #4229, respectively) the peak altitudes of some
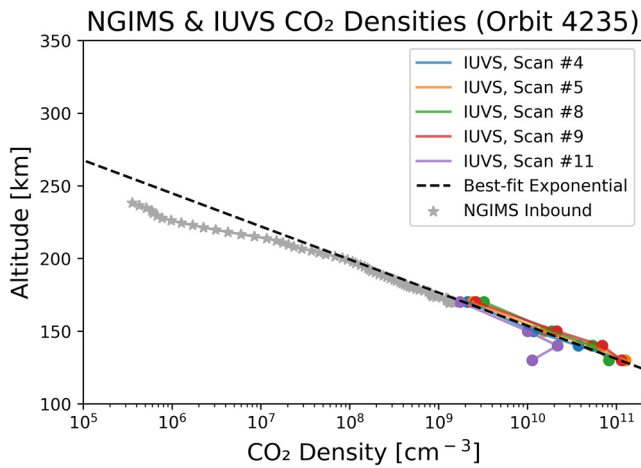
Figure 4. Empirically derived theoretical CO_2 profile used by models for the data-model comparison (Step 2). This profile was created by fitting a best-fit exponential to the derived Imaging UltraViolet Spectrograph (IUVS) and measured Neutral Gas and Ion Mass Spectrometer (NGIMS) inbound data from this Mars Atmosphere and Volatile EvolutioN (MAVEN) orbit.

background subtracted profiles have been (artificially) slightly shifted down by ~5 km.

4.4. Assumptions/Constraints for Step 2

In Step 2, the models used inputs drawn from observations made by MAVEN (discussed more below). We apply many of the same constraints and assumptions as those applied in Step 1 (i.e., assuming a monoenergetic incident particle beam and monodirectional incident particle movement, and constraining the cross-section processes used). One notable difference in Step 2 is that the models produced outputs at a range of solar zenith angles (i.e., not just at the subsolar point) in order to simulate the different SZAs of each of the IUVS limb scans in this orbit. As in Step 1, we exclude any effects due to electric or magnetic fields.

In order to additionally simplify the inputs for this step, all models assume that the incident particle population is composed entirely of H-ENAs at the top of the atmosphere (i.e., assuming an initial penetrating proton component equal to zero). Based on our findings in Step 1, the proton aurora profile does not significantly change in most models when assuming 100% protons or 100% H-ENAs. Thus, this assumption of particle composition should not significantly affect the final results. The initial H-ENA flux ($F_{H\text{-}ENA}$) is approximated using the equation:

$$F_{H\text{-}ENA} = F_{pp} \times 13.5, \tag{2}$$

where F_{pp} (the orbit mean penetrating proton flux derived from SWIA) equals 2.73×10^6 cm^{-2} s^{-1} in this orbit, and 1/13.5 is the approximate fraction of the incoming beam of H-ENAs that is converted to protons. This conversion value was determined based on previous SWIA observations and the relevant energy-dependent electron stripping and charge exchange cross sections (Halekas, 2017; Halekas et al., 2015), assuming that at the point when H-H$^+$ equilibrium is reached in the collisional atmosphere (i.e., the orbit mean location of the SWIA measurements during orbit periapse) the mix is ~92.5% ENAs and ~7.5% protons (i.e., the equilibrium fractionation for the relevant cross sections at 1 keV).

Another constraint carried over from Step 1 is that all models used the same representative CO_2 density (i.e., a 1 km altitude-binned CO_2 number density profile). However, in Step 2, the theoretical CO_2 density line profile is created based on neutral densities from two MAVEN instruments observing at different altitude ranges during this orbit: IUVS and the NGIMS (Mahaffy et al., 2015). We note that although NGIMS data are acquired during both the inbound and outbound portions of the orbit, we restrict this study to include only inbound data, due to instrument artifacts which have been found to artificially increase CO_2 densities in NGIMS outbound data (e.g., Stone et al., 2018). The IUVS and NGIMS neutral densities are consistent with each other within the limited overlapping altitude range of the two instruments; at a reference altitude of 170 km, the NGIMS CO_2 density is ~1.48×10^9 cm^{-3}, and the smallest derived CO_2 density from different IUVS limb scans is ~1.74×10^9 cm^{-3}.

Figure 4 shows the theoretical CO_2 profile for Step 2, which is created by fitting an exponential to the IUVS and inbound NGIMS data using Equation 1. In this case, $n_{ref} = 1.1 \times 10^{11}$ cm^{-3} (the average IUVS density at reference altitude z_{ref}), $z_{ref} = 130$ km (the minimum altitude observed by IUVS during this orbit). The CO_2 scale height was estimated by varying the temperature value until an appropriate fit was achieved (using a value of $g = 3.41$ m/s^2 at 130 km); a temperature of 180 K was found for the best-fit line. The input parameters used by the models to represent the upstream solar wind and atmospheric conditions in Step 2 are shown in Table 2.

Table 2
Representative Input Parameters for MAVEN/IUVS Orbit #4235 Used in the Data-Model Comparison Step (Step 2)

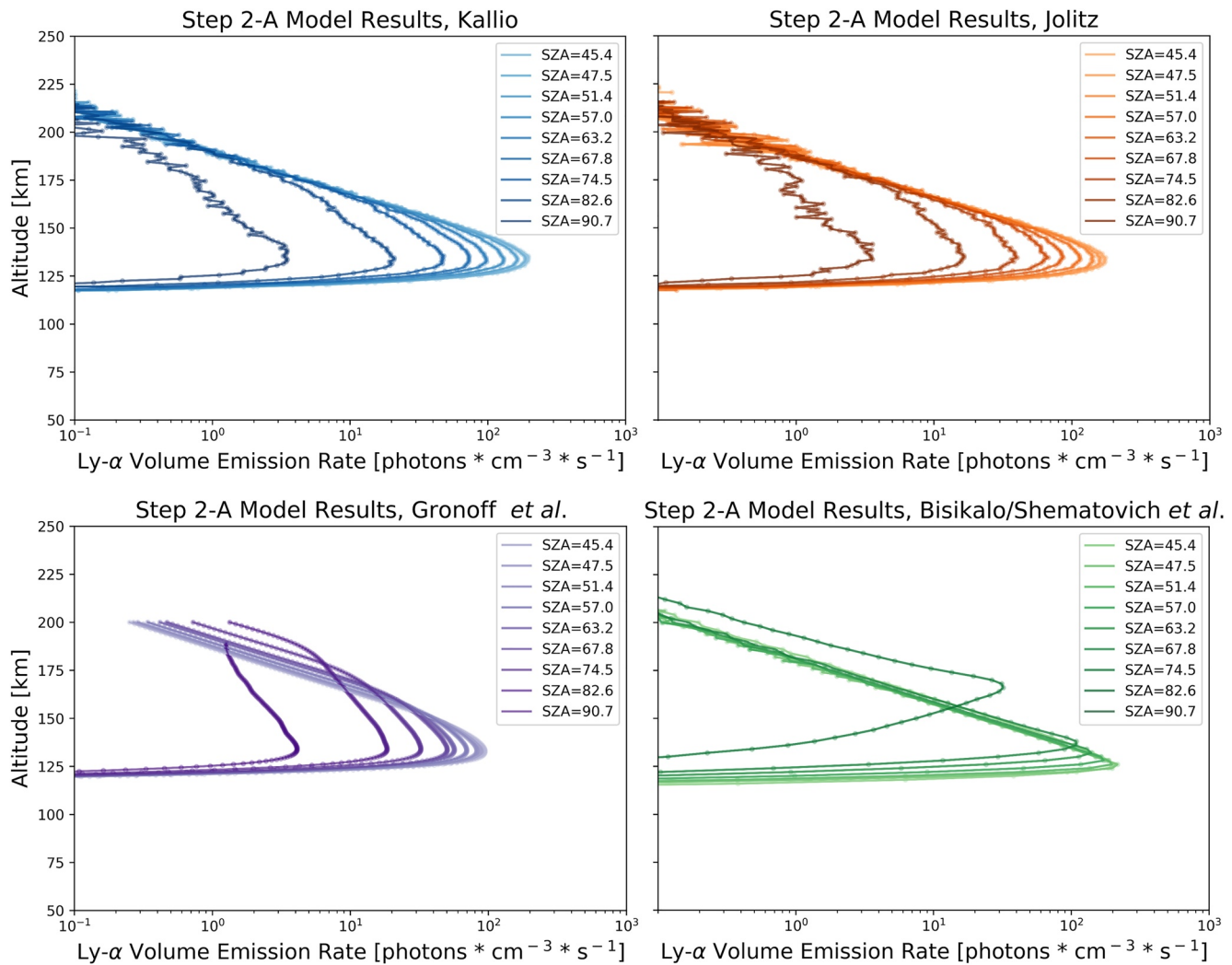|	v [km/s]	$F_{H\text{-}ENA}$ [cm^{-2} s^{-1}]	F_{proton} [cm^{-2} s^{-1}]	Atmospheric temperature (best-fit) [K]
Orbit #4235 Input Parameters	430	3.686×10^7	0	180

Figure 5. Simulation results from the data-model comparison step of the campaign (Step 2-A), showing proton aurora altitude-volume emission rate (VER) profiles from each model for the specified input parameters and solar zenith angles (SZAs). Most model results display similar peak altitudes and VERs agree with each other to within less than an order of magnitude. Note that SZA is decreasing from left-to-right between profiles in each panel.

4.5. Results of Step 2-A

The results of Step 2-A show that all models simulate the input data to within less than an order of magnitude of the same VERs (Figure 5). As in Step 1, the results of Step 2-A also show that the Jolitz and Kallio simulations exhibit the most similarities to each other in terms of VERs and peak altitudes. The Gronoff et al. model results exhibit relatively low VERs compared with other models.

In Step 1, we used the models to simulate a proton aurora profile at a single SZA (i.e., the subsolar point). However, in Step 2, each model simulated proton aurora profiles at numerous SZAs between ~45° and 90°. Thus, in Step 2 we are able to observe the decrease in Ly-α proton aurora brightness associated with increasing SZA. The proton aurora brightness appears to monotonically decrease in the Kallio, Jolitz, and Gronoff et al. simulations (particularly at low SZAs), but in the Bisikalo/Shematovich et al. simulation results the decrease is more gradual at lower SZAs (and pronounced at higher SZAs).

We note that the Bisikalo/Shematovich et al. Monte Carlo calculations for the two highest SZA profiles (i.e., SZA = 82.6° and 90.7°) resulted in practically no Ly-α excitations, hence their absence on the plots in Figures 5 and 6. The Bisikalo/Shematovich et al. model results also exhibit relatively low peak altitudes at lower SZAs in comparison with other models; however, this model is the only one showing variability in the
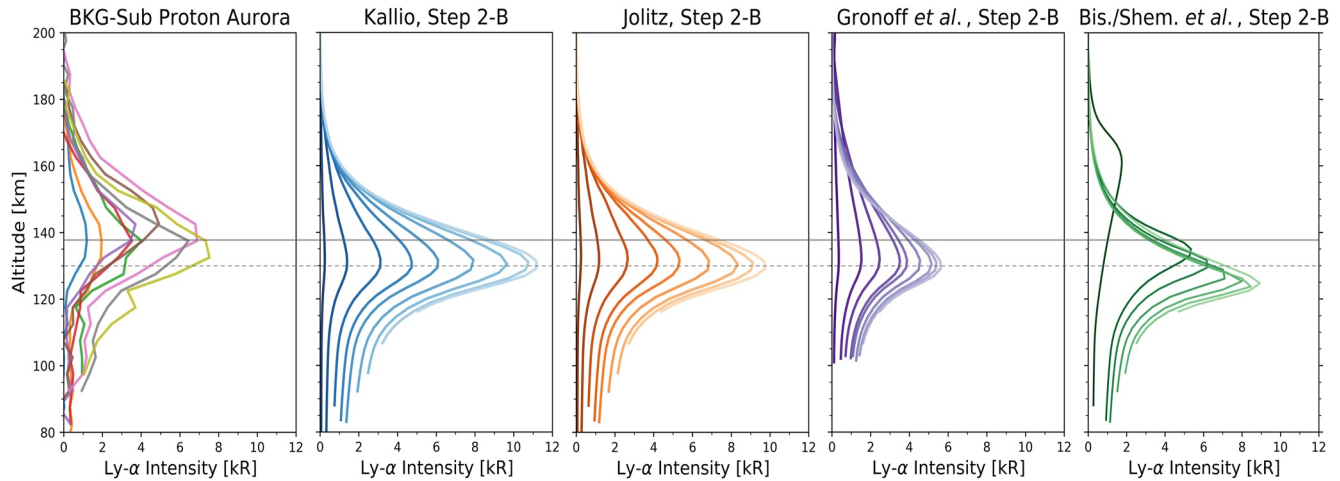
Figure 6. Simulation results for the data-model comparison after running the results through the radiative transfer model (Step 2-B). The background-subtracted (i.e., after subtracting out the theoretical "background" coronal H contribution) altitude-intensity profiles for this orbit are shown on the far left plot for comparison. The simulated proton aurora Ly-α intensities from each of the model results closely correlate with the data. However, note that there is still a discrepancy between the average peak altitude of the data profiles (solid gray horizontal line) and the average peak altitude of the model profiles (dashed gray horizontal line). Note also that the solar zenith angle (SZA) of the observations is decreasing from left to right in all plots from SZA ∼90° to SZA ∼45° (i.e., moving toward the subsolar point), as shown in Figures 3 and 5 legend.

peak altitudes between SZA profiles. In this 1-D kinetic model, Ly-α photons are excited in local collisions of H-ENAs with the ambient atmospheric gas and the VERs are accumulated for the projection velocities of H-ENAs into the given SZA direction. In the case of high SZAs, the Ly-α excitations are caused mainly by the H-ENAs moving in the tangential trajectories relative to the upper atmosphere, which do not penetrate deep into the atmosphere. This results in: (a) very low values of Ly-α VERs for high SZAs (especially for runs with SZA = 82.6° and 90.7°); and (b) an increase of the peak height of the profiles with SZA (i.e., because the kinetic energy of collisions becomes lower for the excitation collisions along the tangential trajectories of the H-ENAs).

4.6. Results of Step 2-B

Forward-modeling the simulation results using the radiative transfer model in Step 2-B allows a more direct comparison between the model results and the IUVS data. In so doing, we find through Step 2-B that the models effectively reproduce the general shape of the data, with some models overestimating and some underestimating the proton aurora brightness (Figure 6). All of the peak altitudes from the model results are ∼5–15 km lower than the observed peak altitudes. The simulated intensities of the Gronoff et al. and Bisikalo/Shematovich et al. model results for the low SZA profiles (i.e., profiles on the right-most side of each plot) are ∼1–1.5 kR higher and lower (respectively) than the proton aurora intensities observed in the data for similar SZA profiles. However, at high SZAs, all three models for which profiles exist appear to simulate the data intensities effectively. The Kallio and Jolitz model intensities overestimate the data by a few kR at low SZAs, while the Gronoff et al. model intensities underestimate by a few kR. At low SZAs, the Bisikalo/Shematovich et al. model intensities closely correlate with the data intensities, but still slightly overestimate the data; however, the Bisikalo/Shematovich et al. intensities underestimate the data at high SZAs. While all models effectively simulate the shape and SZA variability of the data profiles, none of the model intensities match the data exactly (possible reasons for this discrepancy are discussed in the following section).

Significant peak altitude discrepancies between the models and the data are present in every model. This altitude discrepancy suggests that other processes/assumptions are not fully accounted for or understood in our evaluation of the results. In the following section, we examine numerous possible parameters that may contribute to the observed discrepancies between the data and the models.
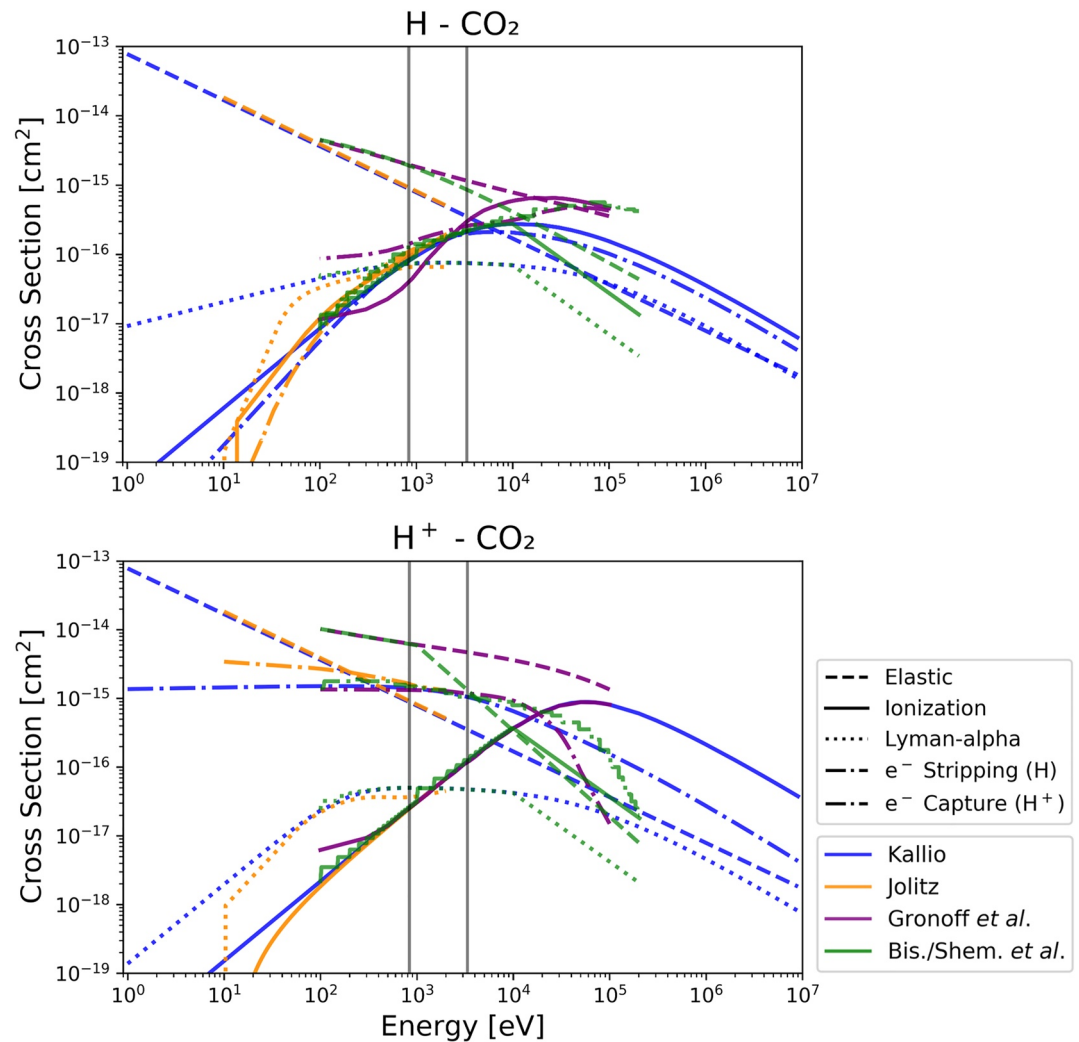
Figure 7. Available cross-section values used by each modeling team (denoted by color) for the five different overlapping cross-section processes considered in this study (denoted by line style). The solid vertical lines (gray) indicate the energy ranges evaluated in the representative cases in Step 1 assuming average (400 km/s) and high (800 km/s) solar wind velocities. See Table S1 in Supporting Information S1 for more information regarding the cross-section processes and relevant references in each model.

5. Discussion of Parameters Affecting Model Differences and Data-Model Discrepancies

5.1. Cross-Section Processes and Scattering Angle Distributions

Differences in cross section and DSCS values are a probable partial contributor to the differences in the results simulated by each model. While the models in this study utilize the same five processes, most models do not use the same cross sections (see Figure 7 and Table S1 in Supporting Information S1 for details). As shown in Figure 7, these values can change significantly with varying energy ranges. The cross-section values used in each model agree to within less than an order of magnitude of each other for the relevant energy range in this study (i.e., 100 eV–2 keV). The most variable cross section across the models were those used for elastic collisions, with elastic cross sections used by the Bisikalo/Shematovich et al. and Gronoff et al. models exceeding those used by the Kallio and Jolitz models by a factor of ∼5–8. These differences can cause notable inter-model variability. Since many processes have not been measured in a laboratory for proton/H collisions with CO_2, an interpolated or substitute value is used for protons/H with O_2 or N_2. Particularly few measurements of protons with CO_2 are available for Ly-α. Comparable cross-section values are a likely cause for the similarities observed between the Jolitz

and Kallio results, and also a likely cause for the minor variability between these two models in the data-model comparison, as the Jolitz model uses smaller Ly-α cross sections at low energies and exhibits intensities that are 1–2 kR smaller than those of the Kallio model at low SZAs.

Different implementations of scattering can also cause inter-model variations. A model that assumes that a particle travels in the same direction before and after a collision ("forward scattering") will predict deeper particle penetration than a model that predicts variability in scattering angle. Introducing even a small probability of non-forward scattering reduces the precipitating flux and resulting emission rate. This is done by converting measured DSCS into a phase function evaluated during a model run. In this study, each model uses different ways to predict scattering (see Text S1–S4 in Supporting Information S1 for detailed model descriptions). Kallio and Jolitz use the same phase function to predict nonzero scattering angles after elastic collisions, while all other collisions are assumed to be forward scattering. This, in tandem with the same model approach (3-D Monte Carlo) likely contributes to their similar model predictions. In contrast, the two 1-D kinetic Boltzmann solver models have slightly different scattering models. Gronoff et al. uses a screened Rutherford phase function with a fixed screening parameter in charge transfer and elastic collisions and assumes forward scattering in ionization collisions. Bisikalo/Shematovich et al. uses the same assumptions for all collisions except charge transfer, for which the model uses energy-dependent DSCS. The inclusion of non-forward scattering in these 1-D models could be responsible for the lower intensities predicted by these models compared to those predicted by the 3-D Monte Carlo models.

5.2. Data Quality and Caveats

In addition to the possible sources of discrepancy in the model assumptions, we must also consider possible caveats associated with the datasets. Because IUVS is a remote sensing instrument, its limb scan observations are created by integrating along the line of sight of the instrument. However, the SWIA penetrating proton fluxes are measured in situ during periapsis, and the orbit averaged value is used in this study. Because of the uniform nature of the processes creating proton aurora across the dayside of the planet it is appropriate to combine these datasets; nevertheless, there may be spatial and/or temporal discrepancies between these observations, even though the data were acquired during the same MAVEN orbit.

Second, because IUVS Level 1C (L1C) data are processed and altitude-binned, we note that minor discrepancies may be introduced in the Ly-α intensities during the data reduction process. Calibrated IUVS L1C data are reported with a systematic uncertainty between ∼10% and 20% (Mayyasi et al., 2017). As the results of this study are sensitive to the absolute calibration of the instrument, we must also consider any possible uncertainties in the IUVS reported intensities as a potential source of discrepancy in the model-data comparison.

5.3. Other Assumptions

There are a number of additional assumptions in this study that may have led to discrepancies between the models and the data. First, numerous data-driven assumptions are made in creating the theoretical CO_2 density profile for Step 2. Any of three variables could be altered that could in turn significantly affect the proton aurora profile: the energy of the incident particles, the density of the atmosphere at the reference altitude, or the neutral atmospheric scale height. All of these variables affect the peak altitude of the proton aurora profile, while changing the scale height and energy also affects the profile peak intensity (more specifically, changing the scale height can also affect how broad/narrow the profile shape becomes). Observations made by MAVEN/SWIA during this orbit provide confidence that the calculation of particle energy and the assumption of monoenergetic particle behavior are appropriate/accurate, and therefore do not significantly affect the results. However, in this study we determine the atmospheric density at the reference altitude (130 km) by extrapolating from the average derived IUVS Level 2 CO_2 density at 130 km. Because the spherically symmetric CO_2 density profile used by modelers in this study is theoretically derived, inaccuracies in the assumed quantities for reference density or scale height would lead to an inaccurate representation of the atmospheric density profile during this time. Thus, it is possible that the CO_2 density profile is not entirely accurate in representing the atmosphere at this time, possibly contributing to some of the discrepancies observed in the data-model comparison. Moreover, only one neutral species (CO_2) is considered in our models, whereas other minor species (e.g., CO, O_2, and O) should also contribute to some extent to the observed profiles in a potentially important way (depending on altitude and latitude/longitude). Since H^+/H cross sections can vary significantly both in peak energy and intensity depending on the target neutral species, the modeling results presented may be modified further if these species are included. We note, however, that

because CO_2 is the overwhelmingly dominant species in the Martian atmosphere, the inclusion of minor species should not alter any of the primary findings presented in this study, but may decrease the observed discrepancies between the data and models. Such an added complexity is outside the scope of the present study and a more in-depth investigation of the inter-model's sensitivity to the neutral atmosphere composition is left for the future.

For simplicity in Step 2 we assume that the precipitating particle population at the top of each model atmosphere is entirely composed of H-ENAs. Although the incident particle population is indeed comprised of a fractionated portion of both ENAs and protons, this simplified assumption is preferred over a nonempirical assumption of an estimated fractionation ratio. Moreover, as the results in Step 1 do not significantly change in most models based on the assumption of an entirely H-ENA- or proton-rich population, we would not expect the effects of this assumption on its own to have a significant impact on the final results. One potential exception may be for the Bisikalo/Shematovich et al. results in which the peak intensity somewhat increases if a particle population of entirely protons is assumed (as seen in Step 1-A and 1-B). Because the Bisikalo/Shematovich et al. results showed slight variability based on the assumed incident particle population, it is possible that the intensities in their model results might be larger if this assumption is changed (which may cause their simulated intensities to more closely resemble those of the Kallio and Jolitz models, but to further overestimate the data intensities in Step 2).

The chosen method for calculating the ENA flux may be a contributor to the observed discrepancies between the data and model intensities. The H-ENA flux used in Step 2 is calculated as an empirically derived multiple of the orbit-averaged SWIA penetrating proton flux. While this ratio is supported by previous SWIA observations (Halekas, 2017; Halekas et al., 2015), the value can vary based on seasonal or other changes (e.g., the solar wind proton flux, the neutral atmospheric scale height, or the location of the bow shock). As determined in Step 1, decreasing the flux by an order of magnitude (which is the typical variability observed throughout a Martian year, e.g., Halekas, 2017) will correspondingly decrease the proton aurora peak intensity by an order of magnitude. Thus, although the method used to calculate the ENA flux is believed to be an accurate and statistically robust approximation, any major deviation from the statistical norm of local conditions during this orbit would cause discrepancies in accurately calculating the H-ENA flux.

Another possible contributor to the data-model discrepancies is the assumption of the monodirectional movement of the incident particles in the atmosphere. We include a terminology note here that in specifying "monodirectional" particle movement, we refer to the bulk velocity (i.e., average speed and direction) of the precipitating particles. All modeling teams represented the incident precipitating particles as having a velocity fixed in magnitude (e.g., 400 km/s and 800 km/s) and direction (anti-sunward). However, in reality the incident solar wind has nonzero temperature, and has a broader variability than modeled. While some model teams investigated the potential effects of this variability on the proton aurora profile (e.g., Figure S4 in Supporting Information S1), the results are preliminary and will be reviewed in further detail in a future study.

In this study, we do not consider the effects of electric or magnetic fields (i.e., IMF, induced, and/or crustal magnetic fields) on proton aurora. While most of the models do not predict any likely significant change on the proton aurora profile caused by magnetic fields, a previous modeling study by Gérard et al. (2019) (which utilized the Bisikalo/Shematovich et al. proton/hydrogen precipitation model) predicted a decrease in the peak brightness of the proton aurora profile in the presence of an induced magnetic field on the order of tens of nT. Comparatively, a recent study by Henderson et al. (2022) that evaluated the effects of magnetic fields on MAVEN/SWIA observations of penetrating protons suggests that only the very strongest magnetic fields with strengths greater than 200 nT are expected to have a notable influence on penetrating proton fluxes (i.e., they did not find a significant influence for magnetic field strengths on the order of 10 nT). Since the IMF magnitude during the MAVEN orbit included in this study is non-negligible (i.e., ~10 nT), it is possible that excluding magnetic/electric fields from our study may contribute to some of the observed model-data discrepancies. However, further analysis is required in order to understand the effects of magnetic fields (and variability in field strengths) on the proton aurora profile.

Lastly, we also do not consider the effects of particle backscattering on the results of this study. Because recent SWIA studies have shown that a significant portion of the incident particle population can be backscattered (Girazian & Halekas, 2021), this factor could thereby contribute to the data-model discrepancies, potentially causing a lower observed proton aurora brightness in the data than what is predicted by models. However, determining the relative abundances of the forward- and back-scattered particle populations is outside the purview of this study and thus the potential impacts on model results are not quantified herein.

5.4. Unique Model Capabilities and Insights

As previously stated, the purpose of this campaign is not to identify the best or most accurate model in the study, but rather, to characterize the ways in which each of the models uniquely excel. In this section, we identify aspects of each model that make them distinctively capable in simulating proton aurora observations, as well as reasons for strong agreement/disagreement between the models.

A few important aspects to consider are the cross sections used in each model, the differences in the way the 3-D and 1-D solvers work, and how the relevant physics is treated. The Monte Carlo solving techniques (e.g., collision by collision determinators) and cross sections used in the Kallio and Jolitz models are very similar (e.g., Figure 7 and Table S1 in Supporting Information S1), leading to the observed similarities in their model results. In contrast to these two models, the Bisikalo/Shematovich et al. and Gronoff et al. models generate outputs by solving coupled proton-hydrogen kinetic Boltzmann transport equations. The Bisikalo/Shematovich et al. model, which also uses Monte Carlo solving techniques, likely exhibits different results than the former two models because of the use of different cross sections and 1-D model dimensionality. The Gronoff et al. kinetic transport model uses cross-section values different than those of other models and a unique 1-D multistream kinetic transport solver. Nevertheless, considering the variety of assumptions and technical implementations included in each model, it is striking how well all of the models agree with each other as well as with the data.

The Bisikalo/Shematovich et al. model is the only one to simulate results that display variability with SZA in the profile peak altitude: at low SZAs their simulated peak altitudes are the furthest from the data peak altitudes, but at some higher SZAs their simulated peak altitudes are closest to those of the data out of all models. Their model is unique in its incorporation of the physics associated with this variability. However, we note that the peak altitudes simulated by their model at very high SZAs are considerably higher than those typically observed for proton aurora (Hughes et al., 2019).

The differences between the model results in the data-model comparison step demonstrate the capabilities, assumptions, and methodologies of each of the models. The Gronoff et al. and Bisikalo/Shematovich et al. models seem to be especially apt at approximating the data intensities at lower SZAs (although the Bisikalo/Shematovich et al. simulated intensities diverge the most at high SZAs). All models predict results which appropriately represent the decrease in Ly-α brightness with increasing SZA: the Kallio, Jolitz, and Gronoff et al. models appear to most accurately simulate this intensity falloff. The Bisikalo/Shematovich et al. model appears to be particularly efficient at simulating the relative intensity differences between profiles at lower SZAs, but the Jolitz model appears to be most consistently efficient across all SZAs. While all models are effective at simulating the data, none of the four particle precipitation models—which results are then run through the radiative transport model—can exactly reproduce the analyzed Ly-α peak intensities and altitudes measured by the IUVS instrument during MAVEN orbit #4235. This may indicate that the input parameters may not accurately represent the situation in the presented case, that the cross sections used may contain noticeable inaccuracies, and/or that some physical processes which are not included into the models play an important role in proton aurora formation.

6. Conclusions and Future Work

The results of this modeling campaign provide a new understanding of the primary factors influencing variability in Martian proton aurora. We identify the relative importance of different input parameters on the proton aurora profile, finding the solar wind particle flux and velocity to be the most influential parameters affecting the profile shape, brightness, and peak altitude. Through undertaking this comparative study, we better constrain the driving processes of proton aurora as characterized by each contributing model; additionally, we determine the influence of model capabilities, solving techniques, and input assumptions on effectively reproducing proton aurora observations, and the dominant physics that needs to be incorporated in future modeling studies in order to accurately represent these events. Moreover, the results of this study are applicable more broadly than proton aurora at Mars, as similar auroral processes could occur on any planetary body that exhibits an extensive neutral H corona. Modeling studies such as this one are particularly important in efforts to study planetary bodies with minimal observations or where data are not available, both within our solar system and beyond (e.g., Venus, comets, and exoplanets).

In a future study, we aim to address the effects of magnetic and electric fields on proton aurora. It will also be important to quantify the effect of the backscattered penetrating particle population on the proton aurora profile;

since the models in this study can readily take into account collisional angular redistributions, incorporating these effects into the models would be feasible and relevant. Evaluating the effects of the monodirectional particle movement assumption (e.g., by varying the incident particle bulk velocity/temperature) should also be considered in a future study. We note that this study depends strongly on consideration of the efficiency of charge exchange between protons in the undisturbed solar wind and H in the extended corona, as this is an upper boundary for calculations due to the precipitation of H-ENAs. Therefore, another possible next step for this campaign could be to consider the variations present in an energy spectrum of incident H atoms and protons (i.e., an energy spectrum that is not monoenergetic). Additionally, major changes in the neutral atmospheric scale height (e.g., due to local or global dust storms) can affect absorption by CO_2 on the bottom side of the proton aurora profile. Because absorption of Ly-α by CO_2 becomes significant below the peak of the proton aurora Ly-α emitting layer, it can have a nontrivial effect on proton aurora modeling efforts, potentially causing apparently lower peak intensities and higher peak altitudes in proton aurora profiles. We plan to address these effects of CO_2 absorption on the proton aurora profile in more detail. A future study could also potentially include creating a more detailed neutral model atmosphere to use in the models (e.g., including SZA variability), or perhaps looking at nadir observations of proton aurora, which may help to bridge the gap between in-situ and remote sensing observations. Finally, it would be interesting to expand our analysis to include an "atypical" example of a proton aurora event in the data-modeling portion of the campaign (e.g., nightside detections, spatially and/or temporally varying).

The MAVEN mission continues to make new and exciting observations of Martian proton aurora, and new Mars missions with UV instrument capabilities are also beginning to make contemporaneous observations of these events. As the current solar cycle increases toward solar maximum (a period corresponding with larger and more frequent solar activity), we anticipate that the intensity and frequency of proton aurora events at Mars will also increase correspondingly (Hughes et al., 2019). Thus, it is imperative in our efforts to study proton aurora that we first develop a firm knowledge of the physics and driving processes through modeling these events; this understanding will provide important context for future efforts to effectively model new and unique auroral observations at Mars.

Data Availability Statement

In this study we use MAVEN/IUVS Level 1C version 13 altitude-binned periapsis data. All daytime Level 1C IUVS data products are publicly available from the Planetary Atmospheres node of the Planetary Data System (PDS) (https://pds-atmospheres.nmsu.edu/data_and_services/atmospheres_data/MAVEN/maven_iuvs.html). Similarly, MAVEN/SWIA (https://pds-atmospheres.nmsu.edu/data_and_services/atmospheres_data/MAVEN/swia.html) and MAVEN/NGIMS (https://pds-atmospheres.nmsu.edu/data_and_services/atmospheres_data/MAVEN/ngims.html) data are also available from the PDS. All MAVEN instrument Software Interface Specification (SIS) documents can be found on the beforementioned PDS websites. The ATMOCIAD (Atomic and Molecular Cross section for Ionization and Aurora Database) database used in the Aeroplanets model (Gronoff et al., 2021) is available at https://doi.org/10.5281/zenodo.4632426.

References

Anderson, D. E., & Hord, C. W. (1971). Mariner 6 and 7 ultraviolet spectrometer experiment: Analysis of hydrogen Lyman-alpha data. *Journal of Geophysical Research*, *76*(28), 6666–6673. https://doi.org/10.1029/JA076i028p06666

Bertaux, J.-L., Leblanc, F., Witasse, O., Quemerais, E., Lilensten, J., Stern, S. A., et al. (2005). Discovery of an aurora on Mars. *Nature*, *435*(7043), 790–794. https://doi.org/10.1038/nature03603

Bisikalo, D. V., Shematovich, V. I., Gérard, J.-C., & Hubert, B. (2018). Monte Carlo simulations of the interaction of fast proton and hydrogen atoms with the Martian atmosphere and comparison with in situ measurements. *Journal of Geophysical Research: Space Physics*, *123*(7), 5850–5861. https://doi.org/10.1029/2018ja025400

Chaffin, M. S., Chaufray, J.-Y., Stewart, I., Montmessin, F., Schneider, N. M., & Bertaux, J.-L. (2014). Unexpected variability of Martian hydrogen escape. *Geophysical Research Letters*, *41*(2), 314–320. https://doi.org/10.1002/2013gl058578

Chaffin, M. S., Kass, D. M., Aoki, S., Fedorova, A. A., Deighan, J., Connour, K., et al. (2021). Martian water loss to space enhanced by regional dust storms. *Nature Astronomy*, *5*(10), 1036–1042. https://doi.org/10.1038/s41550-021-01425-w

Clarke, J. T., Bertaux, J. L., Chaufray, J. Y., Gladstone, G. R., Quémerais, E., Wilson, J., & Bhattacharyya, D. (2014). A rapid decrease of the hydrogen corona of Mars. *Geophysical Research Letters*, *41*(22), 8013–8020. https://doi.org/10.1002/2014gl061803

Deighan, J., Jain, S. K., Chaffin, M. S., Fang, X., Halekas, J. S., Clarke, J. T., et al. (2018). Discovery of proton aurora at Mars. *Nature Astronomy*, *2*(10), 802–807. https://doi.org/10.1038/s41550-018-0538-5

England, S. L., Liu, G., Withers, P., Yiğit, E., Lo, D., Jain, S., et al. (2016). Simultaneous observations of atmospheric tides from combined in situ and remote observations at Mars from the MAVEN spacecraft. *Journal of Geophysical Research: Planets*, *121*(4), 594–607. https://doi.org/10.1002/2016je004997

Galand, M., Lilensten, J., Kofman, W., & Lummerzheim, D. (1998). Proton transport model in the ionosphere. 2. Influence of magnetic mirroring and collisions on the angular redistribution in a proton beam. *Annales Geophysicae*, *16*(10), 1308–1321. https://doi.org/10.1007/s00585-998-1308-y

Galand, M., Lilensten, J., Kofman, W., & Sidje, R. B. (1997). Proton transport model in the ionosphere. 1. Multistream approach of the transport equations. *Journal of Geophysics Research*, *102*(A10), 22261–22272. https://doi.org/10.1029/97JA01903

Gérard, J.-C., Hubert, B., Bisikalo, D. V., & Shematovich, V. I. (2000). Lyman-alpha emission in the proton aurora. *Journal of Geophysics Research*, *105*(A7), 15795–15805. https://doi.org/10.1029/1999JA002002

Gérard, J. C., Hubert, B., Ritter, B., Shematovich, V. I., & Bisikalo, D. V. (2019). Lyman-α emission in the Martian proton aurora: Line profile and role of horizontal induced magnetic field. *Icarus*, *321*, 266–271. https://doi.org/10.1016/j.icarus.2018.11.013

Girazian, Z., & Halekas, J. (2021). Precipitating solar wind hydrogen at Mars: Improved calculations of the backscatter and albedo with MAVEN observations. *Journal of Geophysical Research: Planets*, *126*(2), e2020JE006666. https://doi.org/10.1029/2020JE006666

Gronoff, G., Hegyi, B., Simon Wedlund, C., & Lilensten, J. (2021). The ATMOCIAD database. *Zenodo*. https://doi.org/10.5281/zenodo.4632426

Gronoff, G., Simon Wedlund, C., Mertens, C. J., Barthélemy, M., Lillis, R. J., & Witasse, O. (2012). Computing uncertainties in ionosphere-airglow models: II. The Martian airglow. *Journal of Geophysical Research*, *117*(May), 17. https://doi.org/10.1029/2011JA017308

Gronoff, G., Simon Wedlund, C., Mertens, C. J., & Lillis, R. J. (2012). Computing uncertainties in ionosphere-airglow models: I. Electron flux and species production uncertainties for Mars. *Journal of Geophysical Research*, *117*(A4), 4306. https://doi.org/10.1029/2011JA016930

Halekas, J. S. (2017). Seasonal variability of the hydrogen exosphere of Mars. *Journal of Geophysical Research: Planets*, *122*(5), 901–911. https://doi.org/10.1002/2017JE005306

Halekas, J. S., Lillis, R. J., Mitchell, D. L., Cravens, T. E., Mazelle, C., Connerney, J. E. P., et al. (2015). MAVEN observations of solar wind hydrogen deposition in the atmosphere of Mars. *Geophysical Research Letters*, *42*(21), 8901–8909. https://doi.org/10.1002/2015GL064693

Halekas, J. S., Taylor, E. R., Dalton, G., Johnson, G., Curtis, D. W., McFadden, J. P., et al. (2013). The solar wind ion analyzer for MAVEN. *Space Science Reviews*, *195*(1–4), 125–151. https://doi.org/10.1007/s11214-013-0029-z

Henderson, S., Halekas, J., Girazian, Z., Espley, J., & Elrod, M. (2022). Influence of magnetic fields on precipitating solar wind hydrogen at Mars. *Geophysical Research Letters*, *49*(12), e2022GL099114. https://doi.org/10.1029/2022GL099114

Huestis, D. L., & Berkowitz, J. (2010). Critical evaluation of the photoabsorption cross section of CO_2 from 0.125 to 201.6 nm at room temperature. In *Advances in geosciences, Planetary Science* (Vol. 25: Planetary Science, pp. 229–242). World Scientific.

Hughes, A., Chaffin, M., Mierkiewicz, E., Deighan, J., Jain, S., Schneider, N., et al. (2019). Proton aurora on Mars: A dayside phenomenon pervasive in southern summer. *Journal of Geophysical Research: Space Physics*, *124*, 10533–10548. https://doi.org/10.1029/2019JA027140

Hunten, D. M., Roach, F. E., & Chamberlain, J. W. (1956). A photometric unit for the airglow and aurora. *Journal of Atmospheric and Terrestrial Physics*, *8*(6), 345–346. https://doi.org/10.1016/0021-9169(56)90111-8

Jakosky, B. M., Lin, R. P., Grebowsky, J. M., Luhmann, J. G., Mitchell, D. F., Beutelschies, G., et al. (2015). The Mars atmosphere and volatile evolution (MAVEN) mission. *Space Science Reviews*, *195*(1–4), 3–48. https://doi.org/10.1007/s11214-015-0139-x

Jolitz, R. D., Dong, C. F., Lee, C. O., Lillis, R. J., Brain, D. A., Curry, S. M., et al. (2017). A Monte Carlo model of crustal field influences on solar energetic particle precipitation into the Martian atmosphere. *Journal of Geophysical Research: Space Physics*, *122*(5), 5653–5669. https://doi.org/10.1002/2016JA023781

Jolitz, R. D., Dong, C. F., Rahmati, A., Brain, D. A., Lee, C. O., Lillis, R. J., et al. (2021). Test particle model predictions of SEP electron transport and precipitation at Mars. *Journal of Geophysical Research: Space Physics*, *126*(8), e2021JA029132. https://doi.org/10.1029/2021JA029132

Kallio, E., & Barabash, S. (2000). On the elastic and inelastic collisions between precipitating energetic hydrogen atoms and Martian atmospheric neutrals. *Journal of Geophysical Research*, *105*(24), 973–996. https://doi.org/10.1029/2000ja900077

Kallio, E., & Barabash, S. (2001). Atmospheric effects of precipitating energetic hydrogen atoms on the Martian atmosphere. *Journal of Geophysical Research*, *106*(A1), 165–177. https://doi.org/10.1029/2000JA002003

Lo, D. Y., Yelle, R. V., Schneider, N. M., Jain, S. K., Stewart, A. I. F., England, S. L., et al. (2015). Nonmigrating tides in the Martian atmosphere as observed by MAVEN IUVS. *Geophysical Research Letters*, *42*(21), 9057–9063. https://doi.org/10.1002/2015gl066268

Mahaffy, P. R., Benna, M., King, T., Harpold, D. N., Arvey, R., Barciniak, M., et al. (2015). The neutral gas and ion mass spectrometer on the Mars atmosphere and volatile evolution mission. *Space Science Reviews*, *195*(1–4), 49–73. https://doi.org/10.1007/s11214-014-0091-1

Mayyasi, M., Clarke, J., Quémerais, E., Katushkina, O., Bhattacharyya, D., Chaufray, J., et al. (2017). IUVS echelle-mode observations of interplanetary hydrogen: Standard for calibration and reference for cavity variations between Earth and Mars during MAVEN cruise. *Journal of Geophysical Research: Space Physics*, *122*(2), 2089–2105. https://doi.org/10.1002/2016JA023466

McClintock, W. E., Schneider, N. M., Holsclaw, G. M., Clarke, J. T., Hoskins, A. C., Stewart, I., et al. (2015). The Imaging Ultraviolet Spectrograph (IUVS) for the MAVEN mission. *Space Science Reviews*, *195*(1–4), 75–124. https://doi.org/10.1007/s11214-014-0098-7

Ritter, B., Gérard, J.-C., Hubert, B., Rodriguez, L., & Montmessin, F. (2018). Observations of the proton aurora on Mars with SPICAM on board Mars Express. *Geophysical Research Letters*, *45*(2), 612–619. https://doi.org/10.1002/2017GL076235

Schneider, N. M., Deighan, J. I., Jain, S. K., Stiepen, A., Stewart, A. I. F., Larson, D., et al. (2015). Discovery of diffuse aurora on Mars. *Science*, *350*(6261), aad0313. https://doi.org/10.1126/science.aad0313

Shematovich, V. I., Bisikalo, D. V., Diéval, C., Barabash, S., Stenberg, G., Nilsson, H., et al. (2011). Proton and hydrogen atom transport in the Martian upper atmosphere with an induced magnetic field. *Journal of Geophysical Research*, *116*(A11), A11320. https://doi.org/10.1029/2011ja017007

Shematovich, V. I., Bisikalo, D. V., Gérard, J.-C., & Hubert, B. (2019). Kinetic Monte Carlo model of the precipitation of high-energy proton and hydrogen atoms into the Martian atmosphere with taking into account the measured magnetic field. *Astronomy Reports*, *63*(10), 835–845. https://doi.org/10.1134/s1063772919100056

Simon, C. (2006). *Contribution à L'étude Des Entrées d'énergie Solaire Dans L'ionosphère: Ions Doublement Chargés et Transport Cinétique Des Protons – Application à La Terre et à Titan* (PhD thesis). Université Joseph-Fourier – Grenoble I. Retrieved from http://tel.archives-ouvertes.fr/tel-00109802

Simon, C., Lilensten, J., Moen, J., Holmes, J. M., Ogawa, Y., Oksavik, K., & Denig, W. F. (2007). TRANS4: A new coupled electron/proton transport code – Comparison to observations above Svalbard using ESR, DMSP and optical measurements. *Annales Geophysicae*, *25*(March), 661–673. https://doi.org/10.5194/angeo-25-661-2007

Simon Wedlund, C., Gronoff, G., Lilensten, J., Ménager, H., & Barthélemy, M. (2011). Comprehensive calculation of the energy per ion pair or W values for five major planetary upper atmospheres. *Annales Geophysicae*, *29*(January), 187–195. https://doi.org/10.5194/angeo-29-187-2011

Stone, S. W., Yelle, R. V., Benna, M., Elrod, M. K., & Mahaffy, P. R. (2018). Thermal structure of the Martian upper atmosphere from MAVEN-NGIMS. *Journal of Geophysical Research: Planets*, *123*(11), 2842–2867. https://doi.org/10.1029/2018JE005559